Electronic Supplementary Material (ESI) for Journal of Materials Chemistry C.

Improving the thermoelectric performance of Ti-doped NbFeSb by substitutional doping of the Sb atoms with the isoelectric and heavy Bi atoms

Joseph Ngugi Kahiu [1], Samuel Kimani Kihoi [2] and Ho Seong Lee [1,2,*]

[1] Department of Hydrogen and Renewable Energy, Kyungpook National University, 80 Daehak-ro, Buk-gu, Daegu, 41566, Republic of Korea.

[2] School of Materials Science and Engineering, Kyungpook National University

80 Daehak-ro, Buk-gu, Daegu, 41566, Republic of Korea

*hs.lee@knu.ac.kr

Supplementary information

Table S1. Theoretical, experimental, and relative densities of the fabricated $Nb_{0.8}Ti_{0.2}FeSb_{1-x}Bi_x$ samples.

Sample	Theoretical density (g/cm^3)	Experimental density (g/cm^3)	Relative density (%)
x=0.00	8.21	7.95	96.84
x=0.01	8.24	7.96	96.63
x=0.03	8.29	7.98	96.24
x=0.05	8.35	8.03	96.21
x=0.07	8.40	8.05	95.82

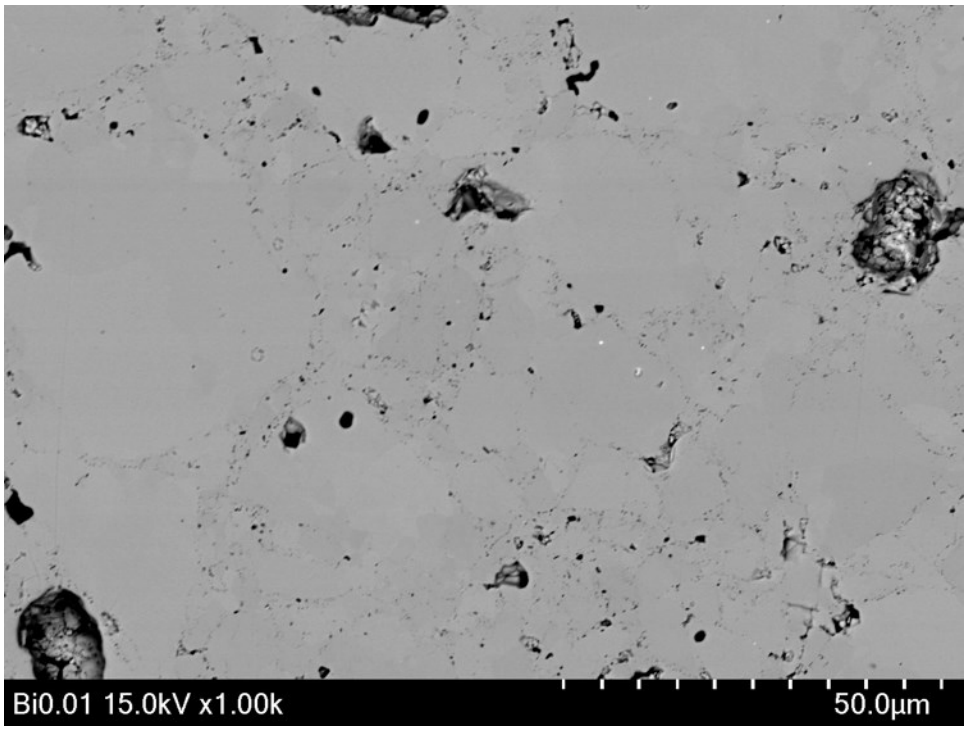

Figure S1. A BSE image of sample x=0.01 showing the sparse Bi precipitates

Sb-deficient samples

The desire to demonstrate the presence and effect of the Sb vacancies on the electronic properties of the Bi-doped samples formed the basis for the synthesis and analysis of the microstructures of the Sb-deficient samples, $Nb_{0.8}Ti_{0.2}FeSb_{1-y}$ (y=0.03,0.05,0.07). The microstructures of the fabricated Sb-deficient samples were analyzed using the FESEM, and thereafter, the electronic properties were measured. Figure S2 shows the microstructures of the fabricated Sb-deficient samples as captured by the FESEM BSE and SE detectors. In Figure S2(a), the microstructure of sample y=0.03 shows scattered dark features that can be identified as pores, as seen in the corresponding SE image in Figure S2(b). Interestingly, similar but intense dark features can be seen in the BSE images of the samples y=0.05 and y=0.07 in Figure S2(c) and (e). However, the corresponding SE images in Figure S2(d) and (f) show that only a few of the dark

features are pores while most that appear in light dark contrast in the SE images are identified as binary Fe_2Nb impurity phases by EDS point analysis. The absence of Fe_2Nb binary impurity phases only in the BSE image of sample y=0.03 in Figure S2(a) highlights the presence of the Sb vacancies. On the contrary, the formation of Fe_2Nb binary phases in the samples y=0.05 and y=0.07 suggests a narrow equilibrium range of Sb vacancies within which the matrix phase is stable. Above this stability range, i.e., in samples y=0.05 and y=0.07, the formation of Fe_2Nb binary phases can be explained on the basis of the law of constant masses as the matrix phases shift to equilibrium.[1]

The effect of the detected Sb vacancies and the observed Fe_2Nb impurity phases on the electronic performance can be seen by comparing the Seebeck coefficient and the electrical conductivity values measured from the Sb deficient samples with those of the sample x=0.00 in Figure S3. Figure S3(a) shows that all the Sb-deficient samples exhibit increased electrical conductivity compared to sample x=0.00. Figure S3(b) shows a reverse trend as a significant decrease in Seebeck coefficient is seen in the Sb-deficient samples. The increase in electrical conductivity and a simultaneous decrease in Seebeck coefficient is consistent with increased majority carrier concentration. Therefore, in addition to confirming the hole-donor role played by the Sb vacancies, the Fe_2Nb Laves phase is shown to play the same role. This agrees with the findings of our previous study, where samples with increased impurity phases, among them Fe_2Nb, demonstrated high values of n.[2] Although a positive effect on the power factor can be seen in Figure S3(c) in sample y=0.03 compared to sample x=0.00, the greatly increased carrier concentration strongly promotes higher electronic thermal conductivity, leading to worse TE performance, as evident in the x=0.07 sample (Figure 7).

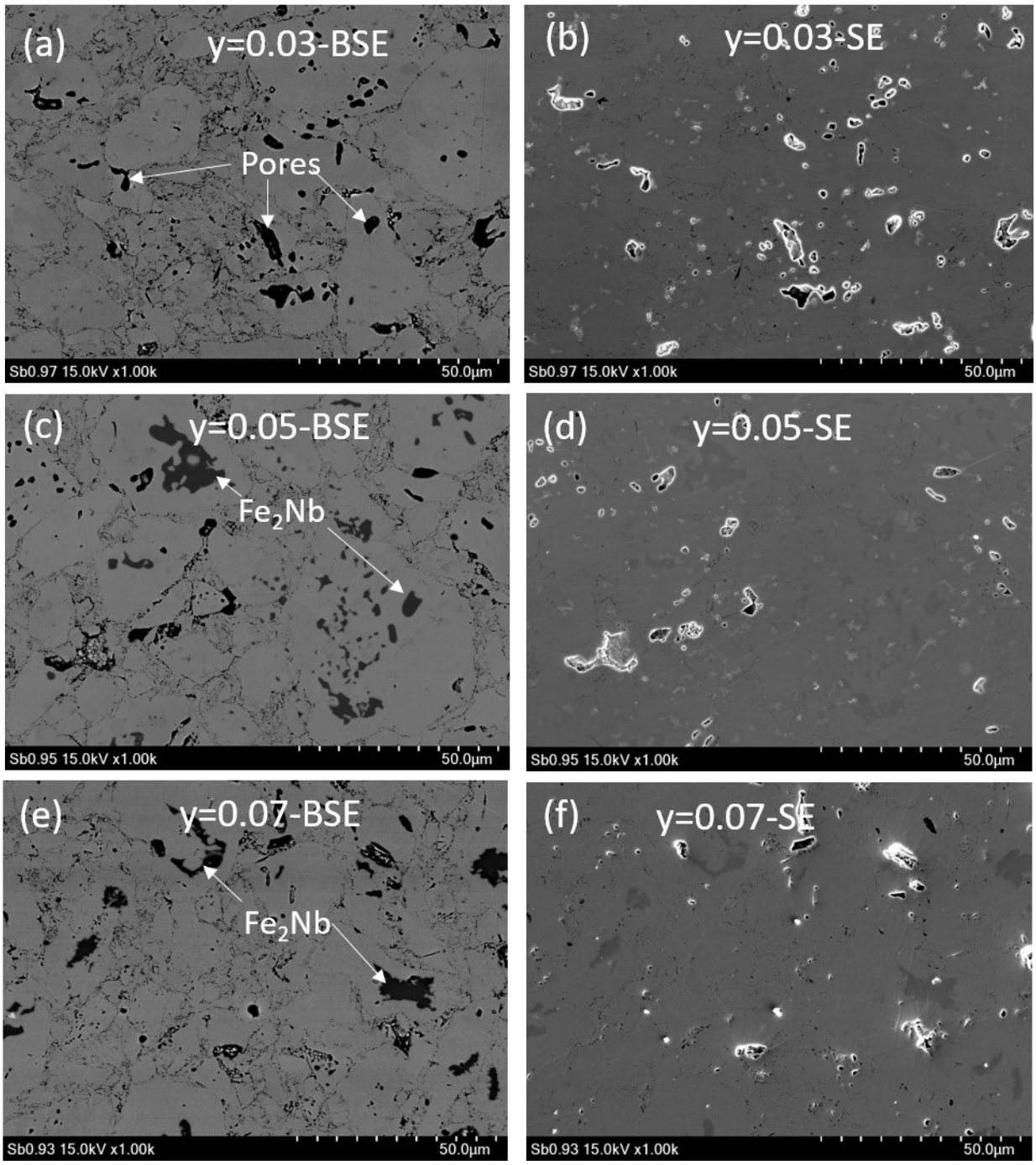

Figure S2. BSE image and corresponding SE image of (a) and (b) y=0.03, (c) and (d) y=0.05, and (e) and (f) y=0.07 samples, respectively.

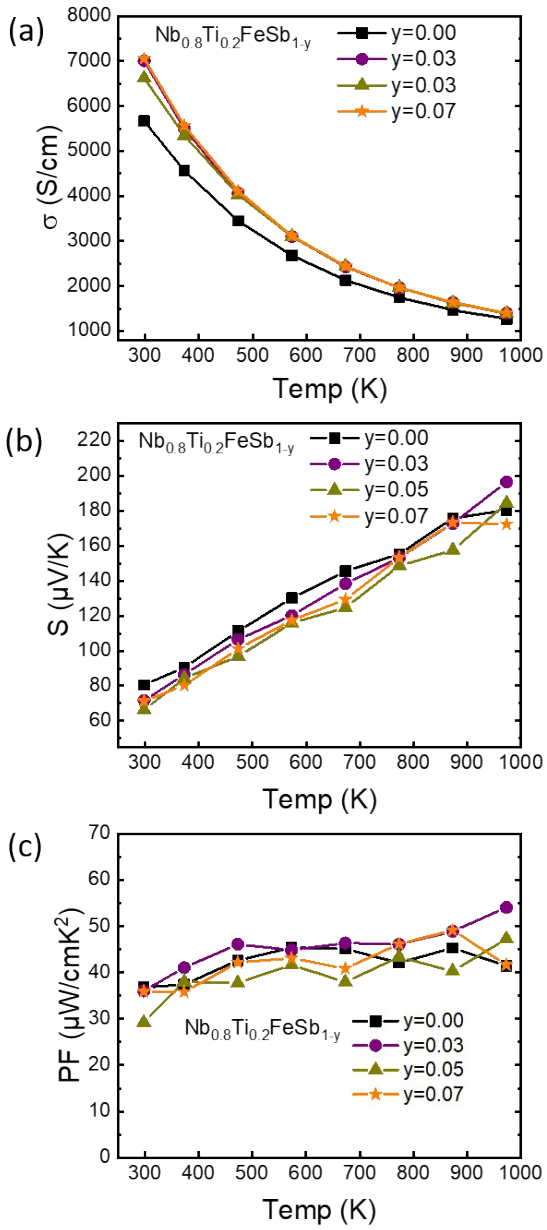

Figure S3. Temperature-dependent (a) electrical conductivities, (b) Seebeck coefficients and (c) power factors of the $Nb_{0.8}Ti_{0.2}FeSb_{1-y}$ samples.

Modeling the lattice thermal conductivity with the model of Debye-Callaway

The model proposed by J. Callaway has become essential for determining the contribution of various scattering parameters to the suppression of lattice thermal conductivity of thermoelectric materials. The model is expressed as:

$$\kappa_{latt} = \frac{k_B}{2\pi^2 v}\left(\frac{k_B T}{\hbar}\right)^3 \int_0^{\theta_D/T} \frac{x^4 e^x}{\tau^{-1}(e^x - 1)^2} dx \quad (1)$$

Where k_B is the Boltzmann constant, $\hbar$ is the reduced Planks constant, $\theta_D$is the Debye temperature, v is the sound velocity, τ is the effective phonon relaxation time, and $x = \hbar\omega/k_B T$.

The effective relaxation time, τ, is expressed as:

$$\tau^{-1} = \tau_{PD}^{-1} + \tau_{3P}^{-1} + \tau_{EP}^{-1} + \tau_{GB}^{-1} \quad (2)$$

Here, the subscripts PD, 3P, EP and GB are pre-factors of point defect scattering, phonon-phonon interactions, electron-phonon interactions, and grain boundary scattering, respectively. It has been shown that the contribution of EP interactions is proportional to the carrier concentration in the form $\tau_{EP}^{-1} \propto n^{4/3}$,[3] while the contribution of grain boundary scattering depends on the grain size in the form $\tau_{GB}^{-1} = v/D$, where D is the average grain size.[4] Because *n* is unchanged within the solubility limit of Bi as a consequence of the isoelectric nature of Bi and Sb and as indicated by the measured Hall data, and because the grain sizes within our samples are assumed to be the same after using an identical synthesis process and conditions, the contributions of electron-phonon interaction and grain boundary scattering are excluded in our model. The τ due to phonon-phonon interactions in half-Heusler compounds is given by;[4]

$$\tau_{3P}^{-1} = Bx^2 \quad (3)$$

Where B is the Umklapp scattering parameter, obtained by He et al. by fitting the thermal conductivity of polycrystalline NbFeSb and interpolating with increasing Ti doping.[5] τ due to point defect scattering is expressed as;

$$\tau_{PD}^{-1} = Ax^2 \, , A = (\frac{k_B T}{\hbar})^4 \frac{V_{at}\Gamma}{4\pi v^3} \tag{4}$$

Where $V_{at}$is the volume per atom and Γ is the disorder scattering parameter obtained by summing the mass fluctuation scattering parameter (Γ_m) and the strain field fluctuation scattering parameter (Γ_s). Detailed expressions for calculating these disorder parameters are clearly outlined in the paper by Yang et al..[6] We estimated the velocity of sound ,v, from the elastic constants measured by Coban et al.[7] Thereafter, the Debye temperature was estimated from the calculated velocity through their relationship expressed as:

$$\theta_D = \frac{\hbar v (6\pi^2 N)^{1/3}}{k_B} \tag{5}$$

Where N is the number of atoms per unit volume.

To investigate the effect of the four different types of scattering centers separately or synergistically, the spectral lattice thermal conductivity (κ_s) is used, which is expressed as:

$$\kappa_s = \frac{k_B}{2\pi^2 v} (\frac{k_B T}{\hbar})^3 \frac{x^4 e^x}{\tau^{-1}(e^x - 1)^2} \tag{5}$$

The contribution of the scattering centers was visualized by plotting κ_s against the ratio of the phonon frequency and Debye frequency (ω/ω_D). The Debye frequency was calculated from its relationship with sound velocity v and the atomic density (n_a) expressed as:

$$\omega_D = \sqrt[3]{6\pi^2 n_a v^3} \quad (5)$$

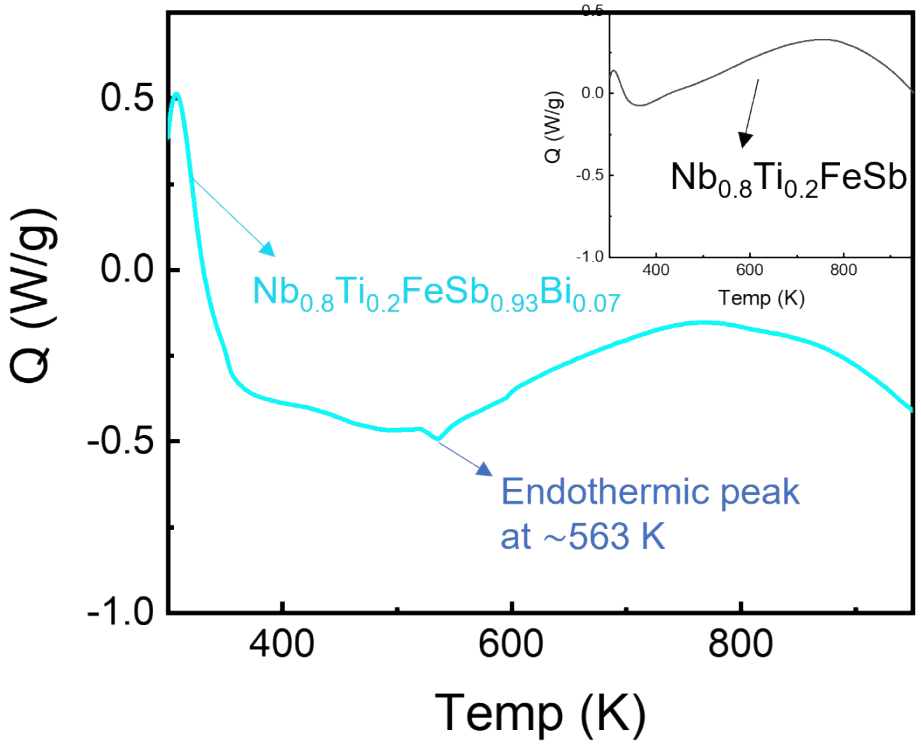

Figure S4. DSC plot of normalized heat flow versus temperature showing an endothermic peak in sample x=0.07 that does not appear in the DSC plot of sample x=0.00 in the inset figure.

References

1 W. D. Callister, *Fundamentals of Materials Science and Engineering: An Integrated Approach,* John Willey & Sons, New York, 2009, pp 180.

2 K. J. Ngugi, W. H. Nam, S. K. Kihoi, H. Kim, J. Ryu, S. Yi and H. S. Lee, *J. Alloys Compd.*, 2021, **871**, 159634.

3 X. Shi, Y. Pei, G. J. Snyder and L. Chen, *Energy Environ. Sci.*, 2011, **4**, 4086–4095.

4 H. Geng, X. Meng, H. Zhang and J. Zhang, *Appl. Phys. Lett.*, 2014, **104**, 202104.

5 R. He, D. Kraemer, J. Mao, L. Zeng, Q. Jie, Y. Lan, C. Li, J. Shuai, H. S. Kim, Y. Liu, D. Broido, C. W. Chu, G. Chen and Z. Ren, *Proc. Natl. Acad. Sci. U. S. A.*, 2016, **113**, 13576–13581.

6 J. Yang, G. P. Meisner and L. Chen, *Appl. Phys. Lett.*, 2004, **85**, 1140–1142.

7 C. Çoban, K. Çolakoɨlu and Y. Çiftçi, *Phys. Scr.*2015, **90**, 095701